

Local equilibrium in liquid phase shock waves

Tage W. Maltby , Bjørn Hafskjold *, Dick Bedeaux, Signe Kjelstrup , and Øivind Wilhelmsen
PoreLab, Department of Chemistry, Norwegian University of Science and Technology, NO-7491 Trondheim, Norway



(Received 19 October 2022; accepted 13 March 2023; published 30 March 2023)

We have assessed the assumption of local thermodynamic equilibrium in a shock wave by comparing local thermodynamic data generated with nonequilibrium molecular dynamics (NEMD) simulations with results from corresponding equilibrium simulations. The shock had a Mach number approximately equal to 2 in a Lennard-Jones spline liquid. We found that the local equilibrium assumption holds perfectly well behind the wave front, and is a very good approximation in the front itself. This was supported by calculations of the excess entropy production in the shock front with four different methods that use the local equilibrium assumption in different ways. Two of the methods assume local equilibrium between excess thermodynamic variables by treating the shock as an interface in Gibbs's sense. The other two methods are based on the local equilibrium assumption in a continuous description of the shock front. We show for the shock studied in this work that all four methods give excess entropy productions that are in excellent agreement, with an average variance of 3.5% for the nonequilibrium molecular dynamics (NEMD) simulations. In addition, we solved the Navier-Stokes (N-S) equations numerically for the same shock wave using an equilibrium equation of state (EoS) based on a recently developed perturbation theory. The results for the density, pressure, and temperature profiles agree well with the profiles from the NEMD simulations. For instance, the shock waves generated in the two simulations travel with almost the same speed; the average absolute Mach-number deviation of the N-S simulations relative to NEMD is 2.6% in the investigated time interval.

DOI: [10.1103/PhysRevE.107.035108](https://doi.org/10.1103/PhysRevE.107.035108)

I. INTRODUCTION

A shock wave appears as a sudden, almost discontinuous change in temperature, pressure, and density traveling at supersonic speed [1]. Shock waves are highly irreversible and the amount of energy they carry can be substantial. They are often generated in explosions, lightning, or by objects moving faster than the speed of sound, such as supersonic aircrafts or bullets. The phenomenon has been of interest in several fields due to its applications and destructive properties. Shock waves have been utilized in medicine, where they can disintegrate kidney stones [2], and in industry, where they are used in processes such as explosive welding and sandalwood oil extraction [3]. They are also highly relevant in aerodynamics, where studies of shock-wave phenomena have increased the understanding of supersonic flows [1]. Thus, a better understanding of the behavior and properties of shock waves will benefit a vast array of scientific fields.

A shock wave is a hydrodynamic phenomenon and variations of the Navier-Stokes (N-S) equations are normally used in modeling and analysis of shock-wave data. The N-S equations require an equation of state (EoS) to represent the thermodynamic properties, and local equilibrium is thus implicitly built into the equations. A key question is then, despite the fact that the shock wave is in *global nonequilibrium*, can one still assume *local equilibrium*? If local equilibrium can be assumed, we can use analytic tools from nonequilibrium

thermodynamics (NET) and the entropy balance equation to map the coupled transport processes and find new constitutive flux-force relations.

Most numerical analyses of shock waves rely on solving conservation equations for mass, momentum, and energy [4]. The applicability of the N-S equations, which include viscous and conductive contributions [5], first implemented by Becker in 1921 [6], has been discussed extensively. It has been found that the shock front computed with the N-S equations is thinner than experimental values [7]. Questions regarding the consistency between the entropy profile and the second law of thermodynamics have also been raised [8]. With the development of computational fluid dynamics (CFD), transient shocks are frequently modeled using the N-S equations [5,9]. Numerous methods have been developed to accomplish this in a robust way numerically, e.g., stable centered numerical difference methods such as the FORCE (first order centred) flux and WENO (weighted essentially nonoscillatory) schemes [9,10]. CFD has been applied to complex phenomena such as the modeling of bubble collapse and multiphase flows in the presence of shock waves [11,12] and has thereby given new insight into these phenomena.

In the second half of the 20th century, molecular dynamics (MD) simulations emerged as a useful tool to study shock waves. Simulations were first performed in one dimension in 1966 by Tsai and Beckett [13]. In 1967, Bird published results using the direct simulation Monte Carlo (DSMC) method with focus on the velocity distribution in a shock wave and the density and temperature profiles in the shock front [7]. At the start of the 1970s, simulations were

*bjorn.hafskjold@ntnu.no

expanded to a three-dimensional Lennard-Jones solid and subsequently to a Lennard-Jones liquid in the late 1970s and early 1980s [14,15]. MD simulations, together with DSMC methods, provided a connection between experimental and theoretical methods [7]. The exact thickness of the shock front was determined by Hoover [15] in 1979. Subsequent work compared NEMD simulations with solutions of the N-S equations. It was found that the N-S equations described shock waves at the atomistic scale reasonably well, although they gave thinner shock fronts than NEMD simulations [16]. DSMC simulations have been in good agreement with NEMD simulations [14].

Whether the same relationships between thermodynamic variables apply at a shock front as in a bulk system at equilibrium, referred to as local equilibrium, is a debated topic in the literature [17–19]. It has been shown that the kinetic energy is equipartitioned in stagnant bulk liquids, even with extreme gradients in thermodynamic properties [20], but this is not the case in a shock front where the kinetic temperature computed from the velocity component in the direction of the shock propagation differs from the other temperature components [17]. The anisotropy of the kinetic energy at the shock front and the rapid processes involved challenge the validity of the local equilibrium assumption. In Section IV A we consider the shock as a wave with continuously varying properties across the front and evaluate the local equilibrium assumption by comparing the internal energy computed in small volume elements in the shock with values for equilibrium states at the same temperatures and densities as in the shock.

A key element in this work is the combined use of NEMD and the N-S simulations. We implicitly impose local equilibrium when solving the N-S equations by using a bulk equation of state. This gives us an alternative route to the shock-wave properties. Comparing results from NEMD and solutions of the N-S equations then allows us to discuss the impact of deviations from local equilibrium in the continuous description of the shock front in Sec. IV B.

The entropy production in the shock wave is a useful probe to examine the assumption of local equilibrium. In this work, we present new analyses for the liquid-phase regime. A shock in a liquid phase at a given Mach number propagates significantly faster and is expected to have a smaller thickness than a shock in the gas phase [21]. Local equilibrium is a prerequisite for the use of NET [17–19]. NET is based on an entropy balance in addition to mass, momentum, and energy balances, and provides consistent transport laws for heat and mass transfer and how they couple [22]. Due to the large gradients across the shock front, coupling between heat and mass transfer is arguably likely to be more significant than in homogeneous systems. Our long-term motivation for the present work is to find a more detailed description of energy conversions and coupling between transport processes; we believe that this approach can add significant information to the understanding of shock waves.

In Sec. IV C, we discuss the entropy production in the shock front using four different methods. Two of the methods assume local equilibrium between excess thermodynamic variables by treating the shock as an interface in Gibbs’s sense. The two other methods apply the local equilibrium assumption as if the shock were a bulk system. These

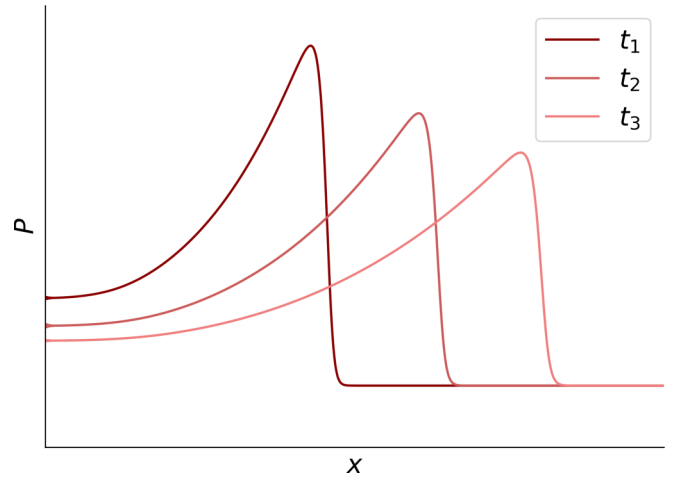


FIG. 1. Visualization of the trace of the pressure tensor of a planar shock propagating in the x direction through a liquid. The three plots represent three times, $t_1 < t_2 < t_3$.

methods were previously evaluated with NEMD simulations of a gaseous Lennard-Jones spline (LJs) fluid [18], where we found that the methods agreed within the combined uncertainties, and the method that treats the shock as an autonomous surface was deemed to be most robust.

II. THE ENTROPY PRODUCTION IN ONE-DIMENSIONAL SHOCKS

We consider a planar shock wave propagating in the x direction through a single-component fluid. The shock was generated by a rapid hot source at time $t = 0$ and position $x = 0$. The system is open and with mirror symmetry around $x = 0$ such that a property at position x and time t has the same value at position $-x$ at time t . An illustration of a propagating pressure profile for $x > 0$ is shown in Fig. 1. As the shock wave propagates, the total entropy of the system increases, mainly due to the entropy production at the shock front, which can be defined as [18]

$$\sigma_s(t) = \int_{x^d(t)}^{x^u(t)} \sigma_s(x, t) dx, \quad (1)$$

where $\sigma_s(x, t)$ is the local entropy production per unit length. The integration limits $x^d(t)$ and $x^u(t)$ are positions behind (downstream) and in front (upstream) of the shock, respectively, chosen such that they encompass the shock front. From here on, we will not explicitly show the time dependency with the understanding that all properties may depend on time.

We now introduce four methods to compute the entropy production. These methods provide the basis for the discussions in Sec. IV C. In two of the methods (BBM and LIT), we consider the fluid as a bulk system with local equilibrium properties. In the other two methods (SBM and GEM), we take a different approach, namely to consider the shock front as a surface and use NET for surfaces [22].

A. The bulk balance method (BBM)

The local entropy production can be calculated from the entropy balance,

$$\sigma_s = \frac{\partial}{\partial t} \rho_s + \frac{\partial}{\partial x} J_s, \quad (2)$$

where ρ_s is the entropy density and J_s is the entropy flux,

$$J_s = \frac{J'_q}{T} + \rho_s v. \quad (3)$$

Here, J'_q is the measurable heat flux in the x direction, T is the temperature, and v is the x component of the fluid streaming velocity. For simplicity, we shall treat v and the x components of other vectors as scalars unless stated otherwise. In this work, we shall use values for ρ_s given by the EoS at the local density and temperature.

We will refer to this method as the ‘‘bulk balance method’’ (BBM) and denote the result σ_s^{BBM} . Using Eq. (2) in Eq. (1) gives

$$\sigma_s^{\text{BBM}} = \int_{x^d(t)}^{x^u(t)} \left(\frac{\partial}{\partial t} \rho_s + \frac{\partial}{\partial x} J_s \right) dx. \quad (4)$$

We set x^u to be a fixed value at the edge of the system, $x^u = L_x$ (independent of time), use Leibniz’s integration rule for the integration of $\frac{\partial}{\partial t} \rho_s$, and observe that $J_s(L_x) = 0$, which gives

$$\sigma_s^{\text{BBM}} = \frac{d}{dt} \left(\int_{x^d(t)}^{L_x} \rho_s dx \right) + \rho_s(x^d) \frac{dx^d}{dt} - J_s(x^d). \quad (5)$$

For simplicity, we set $x^d = \ell - \Delta$, where ℓ is the position of the surface (see Sec. II C) and Δ is a constant (10 molecular diameters in the present case), so that

$$\frac{dx^d}{dt} = \frac{d\ell}{dt} = v^s, \quad (6)$$

where v^s is the shock-wave velocity.

If we set $x^d = 0$ in Eq. (5), we get the total entropy production in the system. Since $J_s(x = 0) = J_s(x = L_x) = 0$, the total entropy production is

$$\sigma_s = \frac{\partial}{\partial t} \left(\int_0^{L_x} \rho_s dx \right). \quad (7)$$

Most of the entropy is produced at the shock front, but near $x = 0$ the bulk phase has gradients due to heat diffusion resulting from the shock generation. Comparing σ_s^{BBM} with the total entropy production gives an estimate for the fractional amount of entropy produced in the shock front.

B. The linear irreversible thermodynamic (LIT) method

By combining the Gibbs relation with mass, energy, momentum, and entropy balances, the local entropy production can be formulated as

$$\sigma_s = J'_q \frac{\partial}{\partial x} \left(\frac{1}{T} \right) - \frac{1}{T} \Pi_{xx} \frac{\partial v}{\partial x}, \quad (8)$$

where Π_{xx} is the xx component of the viscous pressure tensor, $\Pi_{xx} = -(\frac{4}{3}\eta_S + \eta_B) \frac{\partial v}{\partial x}$ [23–26]. The first term on the right-hand side of Eq. (8) is the entropy production from heat conduction and the second term is the entropy production

from viscous flow. The entropy production in the shock front, σ_s^{LIT} , is found by using Eq. (8) in Eq. (1).

The derivation of Eq. (8) relies on the Gibbs relation; i.e., that the same relationship between key thermodynamic variables applies locally across the shock front as in equilibrium bulk systems. A result of this method is a set of flux-force relations; see Ref. [18]. This is the only method that will be evaluated in this work where neither the entropy nor the entropy density are used explicitly in the equations. All the properties in Eq. (8) can be computed directly in MD simulations.

C. Determining excess densities and surface properties

We now introduce a different approach where we consider the shock front as a surface. This gives two more methods that will be used to compute the surface entropy production. They rely on the framework of surface excess variables. Before discussing these methods in detail, we will give an introduction to excess variables.

The shock front, similarly to the interface between two phases, has sharp gradients between its adjacent bulk phases, and is relatively thin. Using the assumption that thermodynamic relations between surface excess variables remain valid even when the overall system is out of equilibrium, it is possible to treat the shock front as an autonomous thermodynamic system [27,28]. Note that this is a fundamentally different assumption than that of local equilibrium for bulk systems. For instance, for evaporation and condensation, the assumption of local equilibrium between the excess variables has been found to hold at the vapor-liquid surface, while the assumption of local equilibrium between bulk variables does not [29].

Excess densities can be defined following Gibbs [30]. Consider the integral of the difference between the actual local density of some property ‘‘ a ’’, $\rho_a(x)$, and its extrapolated values from both sides of the surface:

$$\rho_a^s = \int_{x^d}^{x^u} [\rho_a(x) - \rho_a^d(x)\Theta(\ell - x) - \rho_a^u(x)\Theta(x - \ell)] dx. \quad (9)$$

Here x^d and x^u are positions in the bulk phases adjacent to the surface, Θ is the Heaviside function, and the superscripts ‘‘d’’ and ‘‘u’’ denote linear fits to the bulk densities downstream and upstream of the surface. The parameter ℓ is the position of the surface. This position is somewhat arbitrary, but we shall in this work use the Gibbs dividing surface to define ℓ . This value of ℓ is found by requiring that the excess molar or mass density ρ^s is zero:

$$\rho^s = \int_{x^d}^{x^u} [\rho(x) - \rho^d(x)\Theta(\ell - x) - \rho^u(x)\Theta(x - \ell)] dx = 0. \quad (10)$$

This construction is illustrated in Fig. 2.

Knowing the location of the surface enables us to determine the shock wave velocity v^s and, if the speed of sound is known, the Mach number at a given time. The Gibbs surface also enables us to calculate excess densities of other properties, such as the excess enthalpy density ρ_h^s , internal energy density ρ_u^s , and entropy density ρ_s^s . The internal energy and enthalpy densities can be calculated directly in NEMD simulations while the entropy has to be computed using an

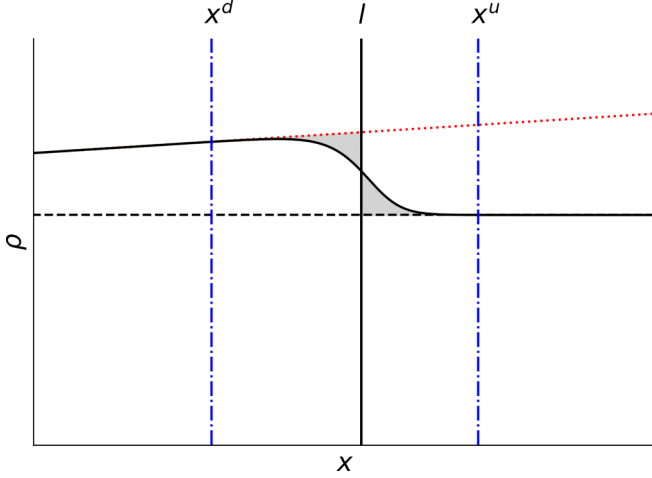


FIG. 2. Illustration of how the Gibbs dividing surface is determined. The black dashed line is the extrapolated upstream bulk density and the red dotted line is the extrapolated downstream bulk density. The blue dash-dot vertical lines show the positions of x^d and x^u and the solid vertical line is the position ℓ of the surface. The etched gray areas represent the integrand in Eq. (10).

equation of state. These properties are then used to compute the corresponding excess properties with Eq. (9).

With the excess internal energy and entropy densities, we can determine the temperature of the surface T^s . Using the integrated form of the Gibbs equation for a surface [22] combined with the Gibbs-Duhem equation yields

$$d\rho_u^s = T^s d\rho_s^s + \mu^s d\rho^s, \quad (11)$$

where μ^s is the excess specific Gibbs energy while ρ_u^s and ρ_s^s are the excess internal energy and entropy densities, respectively. The surface temperature can be determined as ($\rho^s = 0$ by construction of the Gibbs surface)

$$T^s = \left(\frac{\partial \rho_u^s}{\partial \rho_s^s} \right)_{\rho^s}. \quad (12)$$

The surface entropy production discussed in Secs. II A–II B is not the *excess* property in the sense we introduced in Sec. II C. However, comparing the entropy production determined with the different methods is possible because the extrapolated values of the bulk entropy production are approximately zero both from above and below, i.e., $\sigma_s^d \approx \sigma_s^u \approx 0$ (see Fig. 9 in Sec. IV). Substituting the density with the entropy production in Eq. (9) gives Eq. (1) to a good approximation.

D. The surface balance method (SBM)

In the “surface balance method” (SBM) [18], the results from Sec. II C are combined with the entropy balance, Eq. (2). This gives the following expression for the excess surface entropy production:

$$\sigma_s^s = \frac{d\rho_s^s}{dt} + [J_s - v^s \rho_s]_-. \quad (13)$$

We have used the notation $[J_s - v^s \rho_s]_- = (J_s^u - v^s \rho_s^u) - (J_s^d - v^s \rho_s^d)$, which means that the properties in the square

brackets are extrapolated to $x = \ell$ as illustrated in Fig. 2. The SBM relies on properties outside the shock front where local equilibrium holds for the bulk phases. The time derivative of ρ_s^s , which involves the entropy density in the shock front through Eq. (9), is small compared with the other term in Eq. (13). Hence, the SBM is not much affected by any lack of local equilibrium inside the shock front [18].

E. The Gibbs excess method (GEM)

The “Gibbs excess method” (GEM) takes the SBM method a step further by using the Gibbs equation for the surface [18,27]. The excess surface entropy production is then given by

$$\sigma_s^s = [\sigma_q]_- + [\sigma_j]_-, \quad (14)$$

i.e., a sum of the extrapolated local entropy production of the heat flux contribution $[\sigma_q]_- = \sigma_q^u - \sigma_q^d$ and mass flux contribution $[\sigma_j]_- = \sigma_j^u - \sigma_j^d$. The heat term is

$$\sigma_q = J'_q \left(\frac{1}{T} - \frac{1}{T^s} \right) \quad (15)$$

and the mass term is

$$\sigma_j = j \left(s - \frac{1}{T^s} \left[h + \frac{\Pi_{xx}}{\rho} + \frac{1}{2} (v - v^s)^2 \right] \right), \quad (16)$$

where $j = \rho(v - v^s)$ is the mass flux in the shock wave frame of reference, and s and h are the specific entropy and enthalpy, respectively. The GEM method gives detailed information about the energy dissipation in the shock front. It also provides the flux equations; see Ref. [18].

In the GEM method, we utilize properties extrapolated from the bulk phases with the notable exception of the surface temperature, which is computed using excess densities in the shock front. In a previous work, we found that the sum of the properties in the square brackets in Eq. (16) is small [18]. Thus, we have an option to approximate the excess entropy production by changing the mass term to $\sigma_j \approx js$. Since j is continuous across the shock wave, Eq. (16) leads to

$$[\sigma_j]_- \approx j[s]_-, \quad (17)$$

which is the Rankine-Hugoniot (R-H) condition [31,32]. This turns out to be a simple, useful, and accurate approximation, as illustrated in Sec. IV, Fig. 8.

III. SHOCK WAVE SIMULATIONS

A. NEMD simulations

This subsection gives a brief description of how the NEMD simulations were carried out, using an in-house Fortran code. We have employed the Lennard-Jones spline (LJs) potential [33] to represent the intermolecular interactions. Details about the potential and the method can be found in the Supplemental Material (SM) [34] and Ref. [18].

We used an orthogonal box with with $L_x/L_y = L_x/L_z = 16$. A figure showing the system layout is given in the SM. The volume was divided into layers with cross-sectional area $L_y L_z$ and thickness $\Delta x = L_x/256$ so that the volume of each layer was $\Delta x L_y L_z$. In Lennard-Jones units, $\Delta x^* = 1.176$ in this work. The local values of mass and heat fluxes, temperature,

pressure, and other thermodynamic variables were computed in each layer according to the expressions provided in the SM [34] and Ref. [18]. The simulation results are based on 40 parallel runs. Each run had $N = 64\,000$ particles and an overall density $\rho^* = 0.6$, which is a liquid-state density. Thus, each layer contained on average 256 particles.

A simulation run consisted of three steps: (1) an equilibrium simulation to set up the system's state prior to the shock, (2) shock generation, and (3) *NVE* simulations of the shock wave traveling through the box. In Step 1, each parallel was randomized with different numbers of Monte Carlo steps to make the subsequent MD runs statistically independent. At the end of Step 1, the system had a uniform density and temperature $T^* = 2$. In Step 2, a shock wave was created by velocity rescaling the particles in the extreme layers at the left- and right-hand sides of the simulation box (see the SM [34] for an illustration). A certain amount of kinetic energy, 5×10^4 in LJ units, was added to these layers in order to generate a supersonic shock. This was equivalent to heating the layers instantaneously to $T_{\text{boundary}}^* = 135$. The trajectory of the unhindered shock is uniquely determined by the energy of the blast [35]. In Step 3, each of the 40 parallels ran for 10^5 time steps of length $\delta t^* = 0.0002$, with $t^* = 0$ at the start of Step 3.

B. N-S simulations

For the N-S simulations, we solved the balance equations of mass, momentum, and energy:

$$\frac{\partial}{\partial t} \begin{bmatrix} \rho \\ \rho v \\ \rho e \end{bmatrix} + \frac{\partial}{\partial x} \begin{bmatrix} \rho v \\ \rho v^2 + p \\ v(\rho e + p) \end{bmatrix} = \frac{\partial}{\partial x} \begin{bmatrix} 0 \\ (\frac{4}{3}\eta_S + \eta_B)\dot{\epsilon} \\ (\frac{4}{3}\eta_S + \eta_B)v\dot{\epsilon} + \lambda\nabla T \end{bmatrix} \quad (18)$$

where the left-hand side is a vector of the conserved variables, mass density ρ , momentum density ρv , total energy density ρe [9], and pressure p . The total energy density is $\rho e = \rho(u + \frac{v^2}{2})$ where u is the specific internal energy. The right-hand side of Eq. (18) has viscous and conductive contributions, where η_S is the shear viscosity, η_B is the bulk viscosity, $\dot{\epsilon} = \frac{\partial v}{\partial x}$ is the volumetric strain rate, and λ is the thermal conductivity.

To solve this set of partial differential equations, we have applied a finite volume method and integrated in time using an ordinary differential equation integrator. The equations are discretized spatially with the FORCE flux [36]. The formulation is extended with a source term that is discretized with a finite difference method [37].

Equation (18) was evolved in time using an explicit fifth-order Runge Kutta (RK5) integrator [38,39]. The EoS for the LJs fluid used in this work was the uv theory of van Westen and Gross [40,41], accessed through the open-source thermodynamic software THERMOPACK [42]. The EoS was validated with equilibrium MD simulations; see the SM [34]. In the present context, THERMOPACK was used to compute thermodynamic properties for the shock wave using u and ρ from the integration of the N-S equations as input (except for the initial condition, see below). By using the EoS, we implicitly impose local equilibrium when solving Eq. (18).

In order to compare the results from the N-S simulation to those from the NEMD simulation, the N-S initial conditions were taken from the NEMD output from Step 2 discussed in Sec. III A.

Similar to the NEMD simulations, we heated an area with a total thickness of $2\Delta x^* = 2.352$ so that the wave could be followed at comparable times. Also the N-S system was symmetric around $x = 0$. The initial conditions were

$$\begin{aligned} T^*(t = 0, x \leq \Delta x) &= 135, \\ T^*(t = 0, x > \Delta x) &= 2.0, \\ \rho^*(t = 0, \forall x) &= 0.6, \\ v^*(t = 0, \forall x) &= 0, \\ u^*(t = 0, x \leq \Delta x) &= 223. \end{aligned}$$

The internal energy $u^*(x = 0)$ was computed with the EoS using $\rho^* = 0.6$ and $T^* = 135$ as input. The N-S simulations ran for a duration of $t^* = 13.5$ consisting of 4096 equidistantly spaced points and a set of $K = 2161$ temporal points ranging from $t_0^* = 0$ to $t_K^* = 13.5$. The N-S simulations were conducted using real mass-based units and the initial conditions given above were converted to real units using the Lennard-Jones parameters of argon. Once the equations were solved, the results were converted back to dimensionless units. The thermal conductivity and shear and bulk viscosities were determined from independent MD simulations and the shock-wave data as described in the SM [34].

IV. RESULTS AND DISCUSSION

In the following, properties will be reported in dimensionless Lennard-Jones units. A table showing the conversion between SI units and LJ units is given in the SM [34]. Section IV has three main subsections. We first address the question of how well the local thermodynamic properties generated by the NEMD simulations are represented by the corresponding equilibrium values. In the second subsection, we compare the NEMD and N-S results. In the third subsection, we address the entropy production in the shock front and to what extent it can clarify the question of local equilibrium.

Figure 3 shows the NEMD and N-S results for the shock-wave speed as function of time. The wave speed falls about 15% during the time considered in this work.

The potential parameters for argon, $\epsilon/k_B = 124$ K and $\sigma = 3.42 \times 10^{-10}$ m, can serve as an illustration of the conditions used in this work. The equilibrium state ahead of the shock is $T \approx 250$ K and $P \approx 1000$ bar. The blast temperature is $T \approx 17\,000$ K. The shock-front gradients are $dT/dx \approx -5 \times 10^9$ K/m and $dP/dx \approx -2 \times 10^{12}$ bar/m.

A. Local equilibrium

To address the question of local equilibrium in the continuous description of the wave, we have used the method discussed by Tenenbaum *et al.* [43], viz., checking if the equilibrium EoS is satisfied locally in the nonequilibrium state. By ‘‘locally’’ we mean a control volume with enough particles to make computation of thermodynamic properties meaningful and small enough to minimize the effect of gradients in the volume. Hafskjold and Ratkje discussed this for a system with

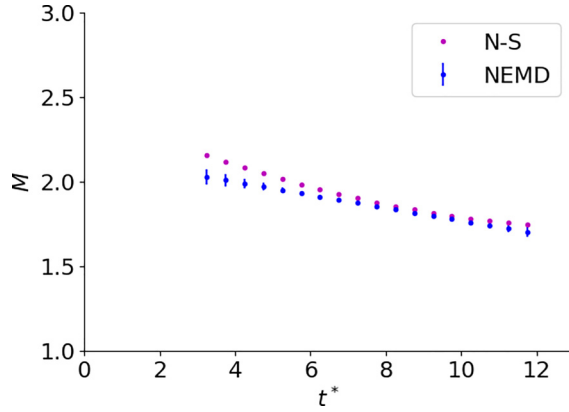


FIG. 3. Mach numbers for the N-S and NEMD data as a function of time. Uncertainties corresponding to three standard deviations were computed by using data from the 40 NEMD parallels.

coupled transport of heat and mass [20]. They found that the condition used by Tenenbaum *et al.* was practical, and we shall use this condition here with Δx as the characteristic thickness of the local volume. Equilibrium data were computed as described in the SM [34].

Figure 4 shows comparisons of the nonequilibrium and equilibrium results for the pressure and specific internal energy at $t^* = 5.75$ and $53 < x^* < 75$. The residual quantities are defined as $P_{\text{res}} = P - P_{\text{ideal}}$ and $u_{\text{res}} = u - u_{\text{ideal}}$. The total pressure and internal energy are measurable quantities which characterize the shock wave. The ideal contribution to the pressure is $P_{\text{ideal}}^* = T^* \rho^*$ and to the specific internal energy it is $u_{\text{ideal}}^* = 3T^*/2$, where T^* is the trace of the temperature tensor. The ideal contributions satisfy equilibrium by definition. The residual properties are more sensitive to deviations from the EoS. Note that the pressure computed by NEMD includes the viscous pressure, which accounts for most of the (small) difference between equilibrium and nonequilibrium. Viscous effects do not affect the internal energy.

The key features of u_{res}^* are (1) it deviates slightly (but more than the combined uncertainties) from the equilibrium values in the shock front (maximum deviation is 0.08 in LJ units), and (2) it matches the equilibrium data immediately behind the front. The second feature means that the surface methods discussed in Secs. II D (SMB) and II E (GEM) are not affected by the lack of equilibrium in the front. It is also worth noting that the EoS deviates slightly from the equilibrium MD results behind the front. Although the deviation is small, it may have an impact on the comparison between NEMD and N-S results.

Another indication of the lack of local equilibrium in the shock front is the nonisotropic kinetic temperature (not shown here). This feature is well known from earlier MD studies [14–17].

The deviations in the shock front show that the “bulk methods” (BBM and LIT) will be affected by this lack of equilibrium, and it remains to be seen how much this changes the entropy production (Sec. IV C).

B. Comparing NEMD and N-S simulations

Figure 5 compares key variables from NEMD and N-S simulations at time $t^* = 5.75$. We remind the reader that local

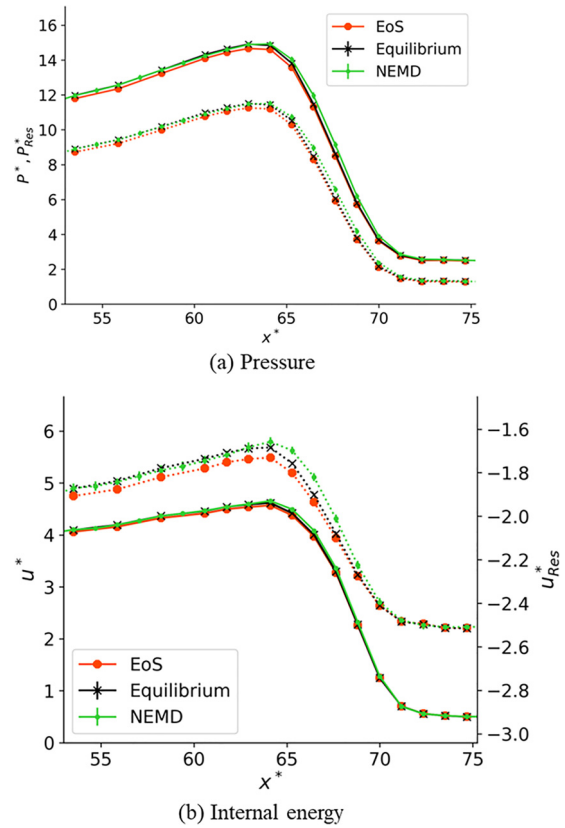


FIG. 4. Examination of the local equilibrium assumption for the pressure and specific internal energy at $t^* = 5.75$. Panel (a) shows the total pressure (upper plots) and the residual pressure (lower plots). Panel (b) shows the specific internal energy (lower plots referring to the left axis) and the residual values (upper plots referring to the right axis). The results labeled “NEMD” are the nonequilibrium values generated in the shock-wave simulation. Results labeled “Equilibrium” are from equilibrium MD simulations and those labeled “EoS” are from the EoS used in the N-S simulations. Uncertainties in the NEMD and MD data shown as error bars are hidden by the size of the symbols in most cases.

equilibrium is not required for the NEMD results, while the N-S results have local equilibrium inherent in the EoS. Profiles for later times are qualitatively similar. Overall, the agreement between N-S and NEMD is very good.

The shock front from the N-S simulations is thinner than from NEMD, as is known from the early MD simulations of shock waves [15]. At time $t^* = 5.75$, the thickness of the NEMD shock was 5.34 in LJ units as computed with the method introduced by Becker [6], whereas the N-S profile had a thickness of 3.62. The difference in shock-wave thickness has been subject to many discussions; see e.g., Velasco and Uribe [26] and references therein. The NEMD temperature is the trace of the temperature tensor, which has different components in longitudinal and transverse directions and consequently a wider front.

The density and pressure decline rapidly behind the shock front and leave a low-pressure and low-density region at the location of the blast. We did not observe that the pressure falls below the equilibrium pressure ahead of the front. At the time shown in Fig. 5, the temperature at $x = 0$ had fallen from

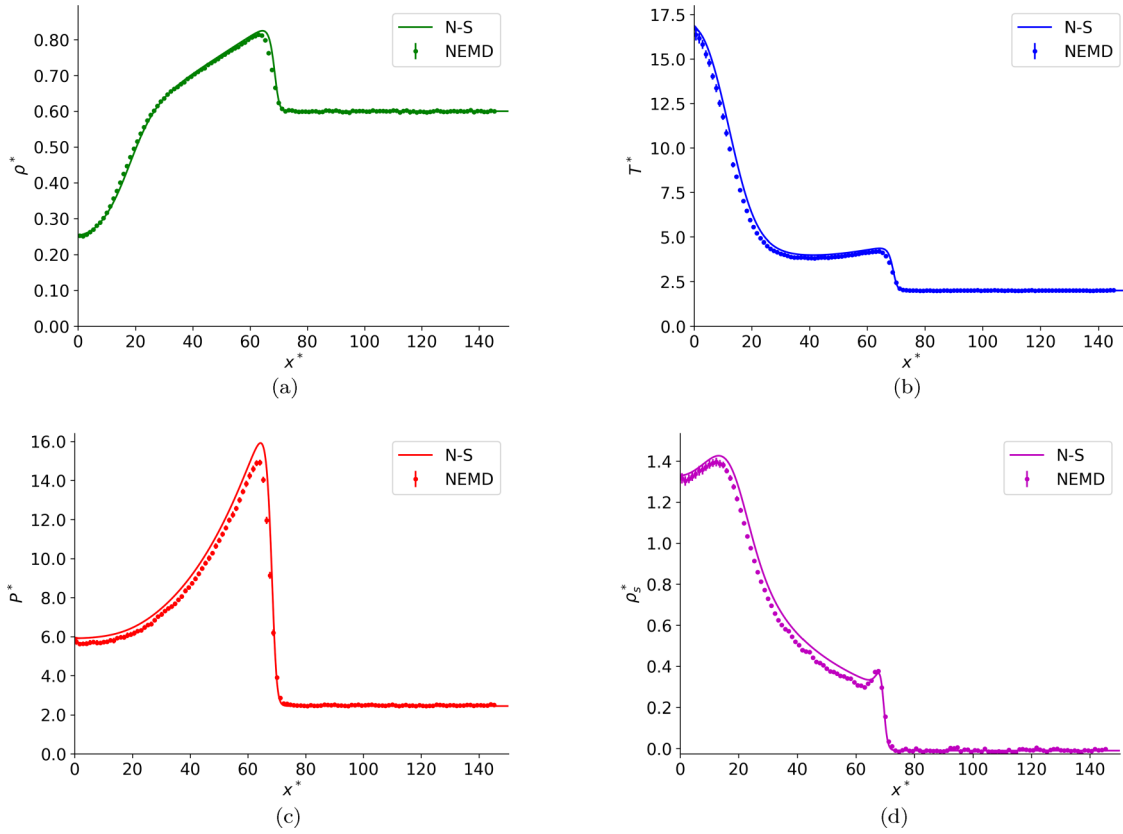


FIG. 5. A comparison of profiles from the NEMD and N-S simulations at $t^* = 5.75$ for (a) density, (b) temperature, (c) pressure, and (d) the entropy density. Panels (b) and (c) show the trace of the temperature- and pressure tensors, respectively. Panel (d) includes the entropy density computed with the equation of state. Uncertainties corresponding to three standard errors were computed using data from the 40 NEMD parallels and are shown as vertical bars on the NEMD results (equal to or smaller than the plot symbols in most cases).

$T^* = 135$ to $T^* \approx 17$ due to expansion and heat diffusion. Note the positive temperature gradient behind the front, leading to a heat flux away from the shock peak (see also Fig. 6).

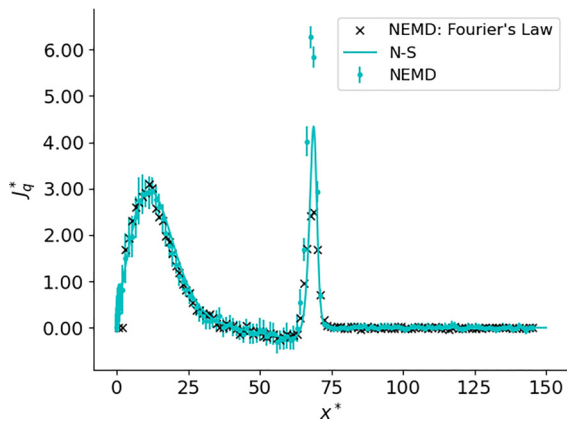


FIG. 6. A comparison of the heat flux from the NEMD and N-S simulations at $t^* = 5.75$. The heat flux computed from Fourier’s law is based on the NEMD temperature data; see text. Uncertainties corresponding to three standard errors were computed using data from the 40 NEMD parallels and are shown as vertical bars on the NEMD results.

Figure 5(b) is interesting as it shows a peak in the entropy density at the peak pressure. This peak is centered nearly at the Gibbs surface (with a difference of $\Delta x^* = 0.11$) and contributes heavily to the excess entropy in the shock front. The entropy density was computed from the EoS since we at the moment have no way to compute the non-equilibrium entropy. Based on the information shown in Fig. 4, we believe the error by so doing to be small. The zero entropy reference state was chosen to be the equilibrium entropy in front of the shock.

Using the density profiles at different times, we determined the shock position by using the definition of the Gibbs surface as described in Sec. II C. The time-dependent positions of the shock from the two simulation methods were nearly identical. The time derivative of these positions was used to calculate the shock velocity. The EoS gave a speed of sound of $v_{\text{sound}}^* = 4.7$ for the equilibrium system in front of the shock. Normalizing the shock velocities with the speed of sound gave the Mach number, M , of approximately 2 (see Fig. 3), which characterizes it as a “weak shock” [19]. The average absolute deviation of the Mach number from the N-S simulations relative to the NEMD simulations for $t^* > 6$ is 2.6%.

The measurable heat flux is shown in Fig. 6. The NEMD data were computed directly as described in the SM [34]. The two other plots involve Fourier’s law: one with N-S as

inherent in the solution method, and the other by using the temperature gradient from NEMD. In both these cases, we used the thermal conductivities determined independently as described in the SM. It seems that Fourier's law does a good job, except in the shock front. The deviations in the front may be due to heat being transported by other mechanisms, e.g., as described by the Cattaneo-Vernotte model [44,45] or the fact that the thermal conductivities we have used are the static values. The reason for the better match between N-S and the direct NEMD can be found in the sharper gradient in the N-S temperatures. Note also the negative heat flux behind the front, which is due to a positive gradient in the temperature profile, Fig. 5(a).

C. Entropy production in the shock-wave front

In two of the methods (BBM, LIT), we consider the fluid as a bulk system. The LIT method is a bit different from the BBM in that the local equilibrium assumption is inherent in the use of the Gibbs equation. Moreover, the LIT method does not use the EoS while the BBM does.

The SBM and GEM are based on a different approach, namely to consider the shock front as a surface and use NET for surfaces. As shown in Sec. IV A, equilibrium is well satisfied on both sides of the front. The only remaining question in this context is the value of T^s , which depends on the surface excess values of the entropy and internal energy densities (implying an integration through the surface). This will be discussed in more detail in Sec. IV C 1.

1. The surface balance method (SBM) and the Gibbs excess method (GEM)

The surface excess internal energy and entropy densities were determined from Eq. (9) using ℓ from the Gibbs dividing surface. The entropy densities were determined using the EoS.

For the SBM, the temporal derivative of the excess entropy density was determined with a linear fit to $\rho_s^s(t)$, using the latter part ($t^* > 8$) of its respective profile. For the NEMD and N-S methods, the downstream properties (ρ_s, J_s) were both extrapolated with a linear function.

The GEM requires values for the surface temperature T^s [Eq. (12)], which was determined by linear regression as illustrated in Fig. 7. The surface temperature for the NEMD shock was determined to be $T_{\text{NEMD}}^{s*} = 2.29 \pm 0.14$ and the N-S equations yielded a surface temperature of $T_{\text{N-S}}^{s*} = 2.20$ [46]. The quantities σ_q and σ_j were extrapolated to the dividing surface to compute the excess entropy production. The dominant term in Eq. (14) is $[\sigma_j]_-$. The downstream extrapolation of σ_j is particularly difficult because of nonlinearity in x . In addition, the enthalpy and kinetic-energy terms in Eq. (16) give a small difference between large numbers, which add substantial noise to $[\sigma_j]_-$. It can be shown, however, that the square-bracketed term in Eq. (16) is zero at steady state [18]. This is why the exact value of T^s is not critical; a $\pm 10\%$ change in T^s changes the value of $[\sigma_j]_-$ by about $\pm 1\%$.

Figure 8 shows the excess entropy production calculated with all four methods plus the R-H approximation. Times $t^* > 5.25$ were investigated since these profiles were in local equilibrium downstream of the shock front, and the wave was far enough from where the shock was generated to not

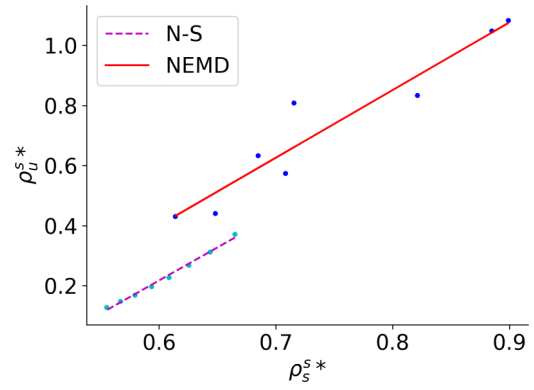
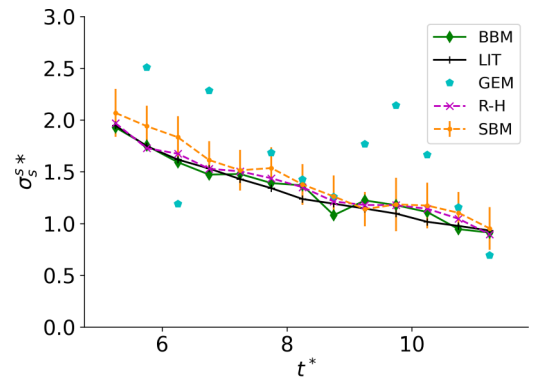
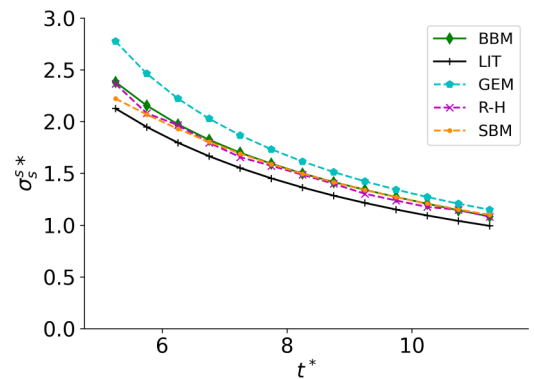


FIG. 7. The excess internal energy plotted against the excess entropy. A linear regression is used to determine the surface temperature T^{s*} which was calculated to be $T_{\text{NEMD}}^{s*} = 2.28$ in the NEMD simulations and $T_{\text{N-S}}^{s*} = 2.20$ in the N-S equations.

obfuscate extrapolations. For the SBM, the results from N-S and NEMD simulations agree within the NEMD uncertainties. The GEM data obtained by NEMD are much more scattered due to noisy extrapolations of σ_j^d .



(a) NEMD simulations



(b) N-S simulations

FIG. 8. Excess entropy production plotted against time for the NEMD (a) and N-S (b) simulations using different methods. For clarity, we have used dashed lines for the surface methods and solid lines for the bulk methods. Uncertainties are three standard errors and were computed using data from 40 NEMD parallels with the SBM method.

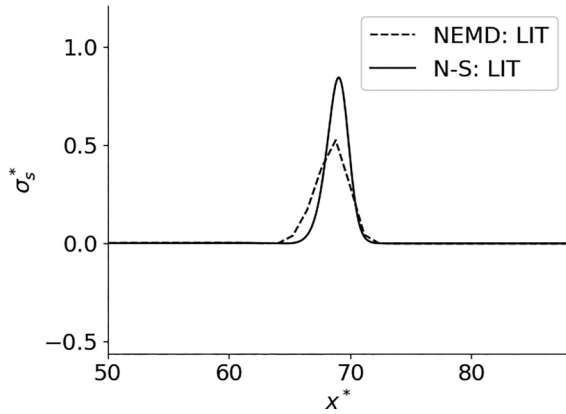


FIG. 9. Local entropy production computed using NEMD- and N-S simulation data with the LIT method as functions of spatial position at time $t^* = 5.75$.

If the shock moves with almost constant speed (cf. Fig. 3), Eq. (17) (R-H) applies, which appears to be an excellent approximation.

2. The linear irreversible thermodynamics (LIT) method and the bulk balance method (BBM)

The local entropy production as determined from Eq. (8), the LIT method, is shown in Fig. 9. Data for the thermal conductivity and the shear and bulk viscosities were determined as described in the SM [34]. The LIT depends on the local equilibrium assumption through the use of the Gibbs equation for the bulk phase. In addition, it makes explicit use of the viscosity. Note that the N-S results are based on a much finer grid in both time and space than the NEMD results. The local entropy production from the LIT method is strictly positive, in accordance with the second law of thermodynamics, and $\sigma_s \approx 0$ outside the shock front. The NEMD and N-S results also manifest the difference in shock-front thickness. The surface entropy production was computed by integrating the local entropy production across the shock front using the composite 1/3 Simpson rule, and the results are shown in Fig. 8.

For the BBM, the entropy density was first integrated in space at different times. Next, a third-order polynomial was regressed to represent the entropy as a function of time. This function was differentiated with respect to time and added to the entropy flux term to give the entropy production. The use of equilibrium values from the EoS apparently has little effect on the entropy production, which means that the BBM is an acceptable route to the shock-wave entropy production. By comparing results from Eqs. (5) and (7), we find that about 80% of the system's total entropy production occurs in the shock front when $t^* > 5.25$.

For the N-S simulations, the excess entropy productions calculated from the different methods are in very good agreement, with an average absolute deviation with respect to the mean value of 3.3% for $t^* > 6$ (3.5% for the NEMD results) [47]. With the accuracy of the simulations presented in this work, we find only small differences between the excess entropy production computed with the four methods. This suggests that local equilibrium is a good approximation for

the continuous description of the shock front. These results agree with recent work by Rauscher *et al.* [48] and with our earlier work for the LJs gas [18].

V. CONCLUSIONS

The main topic for discussion in this work has been the local equilibrium assumption, and whether it applies at the shock front in a liquid. For this purpose, we have simulated a shock wave using nonequilibrium molecular dynamics (NEMD) simulations, and by solving the Navier-Stokes (N-S) equations. The shock was generated by a thermal blast in a one-component liquid consisting of particles interacting with the Lennard-Jones spline (LJs) potential. This resulted in a shock wave with a Mach number of approximately 2.

By comparing the NEMD results with results from equilibrium simulations and the EoS, we have found that equilibrium is satisfied locally, except for small deviations in the shock front (Fig. 4). The surface excess entropy production was determined by use of four different methods for both the NEMD and N-S simulations. Two of the methods, the surface balance method (SBM) and the Gibbs excess method (GEM), depend on the properties adjacent to the shock front, and not explicitly on the front itself. They are therefore insensitive to lack of equilibrium in the shock front and well suited for analyses of the surface excess entropy production. The GEM requires high-quality data for the properties in Eq. (16) and the NEMD results are rather scattered [Fig. 8(a)].

The two methods referred to as the linear irreversible Thermodynamics (LIT) method and the bulk balance method (BBM) both treat the shock front as a continuous profile in intensive variables. We assume in these methods that local equilibrium applies also at the shock front. The BBM gave results in good agreement with with SBM and GEM. When compared with the total entropy production in the whole process, we found that about 80% of the shock's entropy production occurs in the shock front. Overall, the four methods gave consistent excess entropy productions with an average deviation of 3.3% in the time interval considered for the N-S simulations and 3.5% for the NEMD simulations. These deviations are comparable to the uncertainty of the EoS used to describe the properties of the LJs fluid. Our findings confirm the results we found in the previous gas-phase analysis [18], namely that local equilibrium is a good approximation in the continuous description of the shock front also in the liquid phase for a shock with $M \approx 2$.

We implicitly impose local equilibrium when solving the N-S equations. In comparing the NEMD and N-S results we used the Gibbs equimolar surface in both cases. The average absolute deviation of the Mach number from the N-S simulations relative to NEMD was 2.6% in the investigated time interval. Despite their different inherent assumptions, the NEMD and N-S simulations gave very similar density, pressure, and temperature profiles. The N-S equations gave a sharper shock front than the NEMD simulations, which is a characteristic of the N-S equations already documented in the literature. The two methods gave consistent results for the entropy production, which is another indicator of the validity of the local equilibrium assumption.

ACKNOWLEDGMENTS

We thank Dr. Morten Hammer for valuable discussions during the work, Dr. Thuat Trinh for providing viscosity data using LAMMPS, and Dr. Thijs van Westen for discussions on the EoS and uv theory. We acknowledge funding from

the Research Council of Norway, the Center of Excellence Funding Scheme, Project No. 262644, PoreLab. The NEMD simulations were performed on resources provided by the Department of Chemistry at the Norwegian University of Science and Technology (NTNU).

-
- [1] J. D. Andersen, *Fundamentals of Aerodynamics*, 6th ed. (McGraw-Hill, New York, 2017).
- [2] M. Thiel, M. Nieswand, and M. Dörffel, Review: The use of shock waves in medicine—a tool of the modern OR: An overview of basic physical principles, history and research, *Minimally Invasive Ther. Allied Technol.* **9**, 247 (2000).
- [3] R. B. Anoop, K. P. J. Kumar, and A. A. Arjun, A review on applications of shock wave, *Int. Res. J. Eng. Technol.* **6**, 4357 (2019).
- [4] P. O. K. Krehl, *History of Shock Waves, Explosions and Impact A Chronological and Biographical Reference* (Springer-Verlag, Berlin, 2009).
- [5] L. S. García-Colín, R. M. Velasco, and F. J. Uribe, Beyond the Navier-Stokes equations: Burnett hydrodynamics, *Phys. Rep.* **465**, 149 (2008).
- [6] R. Becker, Stosselle und detonation, *Z. Phys.* **8**, 321 (1922).
- [7] G. Bird, The velocity distribution function within a shock wave, *J. Fluid Mech.* **30**, 479 (1967).
- [8] M. Morduchow and P. A. Libby, On a complete solution of the one-dimensional flow equations of a viscous, heat-conducting, compressible gas, *J. Aeronaut. Sci.* **16**, 674 (1949).
- [9] E. F. Toro, *Riemann Solvers and Numerical Methods for Fluid Dynamics*, 3rd ed. (Springer-Verlag, Berlin, 2009).
- [10] G. Jiang and C. Shu, Efficient implementation of weighted ENO schemes, *J. Comput. Phys.* **126**, 202 (1996).
- [11] M. R. Betney, B. Tully, N. A. Hawker, and Y. Ventikos, Computational modelling of the interaction of shock waves with multiple gas-filled bubbles in a liquid, *Phys. Fluids* **27**, 036101 (2015).
- [12] V. Nguyen, T. Phan, and W. Park, Numerical modeling of multiphase compressible flows with the presence of shock waves using an interface-sharpening five-equation model, *Int. J. Multiphase Flow* **135**, 103542 (2021).
- [13] D. H. Tsai and C. W. Beckett, Shock wave propagation in cubic lattices, *J. Geophys. Res.* **71**, 2601 (1966).
- [14] B. L. Holian, Atomistic computer simulations of shock waves, *Shock Waves* **5**, 149 (1995).
- [15] W. G. Hoover, Structure of a Shock-Wave Front in a Liquid, *Phys. Rev. Lett.* **42**, 1531 (1979).
- [16] B. L. Holian, W. G. Hoover, B. Moran, and G. K. Straub, Shock-wave structure via nonequilibrium molecular dynamics and Navier-Stokes continuum mechanics, *Phys. Rev. A* **22**, 2798 (1980).
- [17] B. L. Holian and M. Mareschal, Heat-flow equation motivated by the ideal-gas shock wave, *Phys. Rev. E* **82**, 026707 (2010).
- [18] B. Hafskjold, D. Bedeaux, Ø. Wilhelmsen, and S. Kjelstrup, Theory and simulation of shock waves: Entropy production and energy conversion, *Phys. Rev. E* **104**, 014131 (2021).
- [19] B. Hafskjold, D. Bedeaux, S. Kjelstrup, and Ø. Wilhelmsen, Nonequilibrium thermodynamics of surfaces captures the energy conversions in a shock wave, *Chem. Phys. Lett.* **738**, 100054 (2020).
- [20] B. Hafskjold and S. K. Ratkje, Criteria for local equilibrium in a system with transport of heat and mass, *J. Stat. Phys.* **78**, 463 (1995).
- [21] P. Krehl, *History of Shock Waves* (Elsevier, Amsterdam, 2004), Vol. 1.
- [22] S. Kjelstrup and D. Bedeaux, *Non-Equilibrium Thermodynamics of Heterogeneous Systems* (World scientific, Singapore, 2008).
- [23] R. B. Bird, W. S. Stewart, and E. N. Lightfoot, *Transport Phenomena*, 2nd ed. (Wiley, New York, 2002).
- [24] R. M. Velasco and F. J. Uribe, Shock-wave structure according to a linear irreversible thermodynamic model, *Phys. Rev. E* **99**, 023114 (2019).
- [25] R. M. Velasco and F. J. Uribe, Erratum: Shock-wave structure according to a linear irreversible thermodynamic model [Phys. Rev. E **99**, 023114 (2019)], *Phys. Rev. E* **101**, 019903(E) (2020).
- [26] R. Velasco and F. Uribe, A study on the Holian conjecture and linear irreversible thermodynamics for shock-wave structure, *Wave Motion* **100**, 102684 (2021).
- [27] D. Bedeaux, A. M. Albano, and P. Mazur, Boundary conditions and non-equilibrium thermodynamics, *Physica A* **82**, 438 (1976).
- [28] A. M. Albano and D. Bedeaux, Non-equilibrium electrothermodynamics of polarizable multicomponent fluids with an interface, *Physica A* **147**, 407 (1987).
- [29] Ø. Wilhelmsen, D. Bedeaux, and S. Kjelstrup, Heat and mass transfer through interfaces of nanosized bubbles/droplets: the influence of interface curvature, *Phys. Chem. Chem. Phys.* **16**, 10573 (2014).
- [30] J. W. Gibbs, On the equilibrium of heterogeneous substances, *Am. J. Sci.* **s3-16**, 441 (1878).
- [31] W. J. M. Rankine, XV. On the thermodynamic theory of waves of finite longitudinal disturbance, *Philos. Trans. R. Soc. A* **160**, 277 (1870).
- [32] H. Hugoniot, Mémoire sur la propagation du mouvement dans un fluide indéfini (première partie), *J. Math. Pures Appl.* **3**, 477 (1887).
- [33] B. L. Holian and D. J. Evans, Shear viscosities away from the melting line: A comparison of equilibrium and nonequilibrium molecular dynamics, *J. Chem. Phys.* **78**, 5147 (1983).
- [34] See Supplemental Material at <http://link.aps.org/supplemental/10.1103/PhysRevE.107.035108> for details of the model system used in this work, a table for conversions of variables between reduced Lennard-Jones and SI units, how the simulations were carried out, and the computations of transport coefficients for the Lennard-Jones spline system.

- [35] D. L. Jones, Intermediate strength blast wave, *Phys. Fluids* **11**, 1664 (1968).
- [36] V. A. Titarev and E. F. Toro, Musta schemes for multi-dimensional hyperbolic systems: analysis and improvements, *Int. J. Numer. Methods Fluids* **49**, 117 (2005).
- [37] P. Aursand, M. Hammer, S. T. Munkejord, and Ø. Wilhelmsen, Pipeline transport of CO_2 mixtures: Models for transient simulation, *Int. J. Greenhouse Gas Control* **15**, 174 (2013).
- [38] J. R. Dormand and P. J. Prince, A family of embedded Runge-Kutta formulae, *J. Comput. Appl. Math.* **6**, 19 (1980).
- [39] P. Virtanen, R. Gommers, T. E. Oliphant, M. Haberland, T. Reddy, D. Cournapeau, E. Burovski, P. Peterson, W. Weckesser, J. Bright, S. J. van der Walt, M. Brett, J. Wilson, K. J. Millman, N. Mayorov, A. R. J. Nelson, E. Jones, R. Kern, E. Larson, C. J. Carey *et al.*, SciPy 1.0: Fundamental algorithms for scientific computing in Python, *Nat. Methods* **17**, 261 (2020).
- [40] T. van Westen and J. Gross, Accurate thermodynamics of simple fluids and chain fluids based on first-order perturbation theory and second virial coefficients: uv -theory, *J. Chem. Phys.* **155**, 244501 (2021).
- [41] T. van Westen, M. Hammer, B. Hafskjold, A. Aasen, J. Gross, and Ø. Wilhelmsen, Perturbation theories for fluids with short-ranged attractive forces: A case study of the Lennard-Jones spline fluid, *J. Chem. Phys.* **156**, 104504 (2022).
- [42] Ø. Wilhelmsen, A. Aasen, G. Skaugen, P. Aursand, A. Austegard, E. Aursand, M. Aa. Gjennestad, H. Lund, G. Linga, and M. Hammer, Thermodynamic modeling with equations of state present challenges with established methods, *Ind. Eng. Chem. Res.* **56**, 3503 (2017); <https://github.com/thermotools/thermopack>.
- [43] A. Tenenbaum, G. Ciccotti, and R. Gallico, Stationary nonequilibrium states by molecular dynamics. Fourier's law, *Phys. Rev. A* **25**, 2778 (1982).
- [44] C. Cattaneo, Sulla conduzione del calore, *Atti Sem. Mat. Fis. Univ. Modena* **3**, 83 (1948).
- [45] P. Vernotte, Les paradoxes de la theorie continue de l'equation de la chaleur, *Comptes Rendus* **246**, 3154 (1958).
- [46] The N-S simulation was, unlike the NEMD simulations, only one run, which prevented us from estimating the N-S uncertainty in T_{N-S}^{s*} in the same way as in T_{NEMD}^{s*} . Based on Fig. 7, we believe the uncertainty in T_{N-S}^{s*} to be small.
- [47] Results from the GEM based on the NEMD simulations were not included in this number due to the larger uncertainties in these results, which in part was due to the coarse spatial and temporal grid used in the NEMD simulations.
- [48] P. M. Rauscher, H. C. Öttinger, and J. J. de Pablo, Nonequilibrium statistical thermodynamics of multicomponent interfaces, *Proc. Natl. Acad. Sci. USA* **119**, e2121405119 (2022).